ACS APPLIED MATERIALS & INTERFACES

Research Article

www.acsami.org

Fluorinated Raspberry-like Polymer Particles for Superamphiphobic Coatings

Weijie Jiang, Claudia M. Grozea, Zengqian Shi, and Guojun Liu*

Department of Chemistry, Queen's University, 90 Bader Lane, Kingston, Ontario, Canada K7L 3N6

Supporting Information

ABSTRACT: Raspberry-like (RB) polymer particles were prepared, fluorinated, and cast onto glass plates to yield highly water- and oil-repellant superamphiphobic particulate coatings. To procure the RB particles, glycidyl-bearing 212 and 332 nm particles (abbreviated as *s*-GMA and *l*-GMA, respectively) were first prepared via surfactant-free free radical emulsion polymerization. Reacting the glycidyl groups of the *l*-GMA particles with 2,2′-(ethylenedioxy)bis-(ethylamine) (EDEA) produced large amine-functionalized particles (*l*-NH_2). The *l*-NH_2 particles were then reacted with an excess of the *s*-GMA particles to create RB particles. For surface fluorination, the residual glycidyl groups of the smaller *s*-GMA particles surrounding the central *l*-NH_2 core of the RB particles were first converted to amino groups by reaction with EDEA. The purified amino-bearing particles were subsequently reacted with an excess of a statistical copolymer poly(2-(perfluorooctyl)ethyl methacrylate-*co*-glycidyl methacrylate), P(FOEMA-*co*-GMA). Casting these particles onto glass plates yielded particulate films that exhibited static contact angles of 165 ± 2°, 155 ± 3°, 152 ± 4°, and 143 ± 1° and droplet rolling angles of <1 °, <1 °, 7 ± 2°, and 13 ± 2° for water, diiodomethane, corn-based cooking oil, and hexadecane droplets, respectively. These results demonstrated that this practical bottom-up approach could be used to produce superamphiphobic coatings.

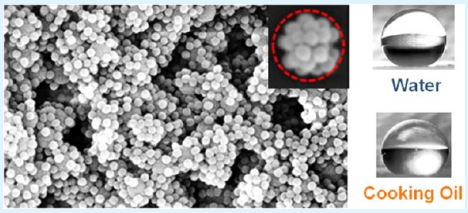

KEYWORDS: *raspberry-like particles, amphiphobic coatings, emulsion polymerization, superhydrophobicity, oil repellency, fluorinated bifunctional copolymer*

I. INTRODUCTION

Coatings that repel both water and oil are omniphobic or amphiphobic. Amphiphobic coatings that possess water and oil contact angles that both exceed 150 ° and rolling angles below 10 ° are superamphiphobic.[1−8] On superamphiphobic surfaces, oil- and water-borne contaminants bead up and roll off readily, taking dust particles and dirt along with them. A superamphiphobic surface will thus remain clean for a longer time than an untreated surface. In addition, superamphiphobic coatings protect metal substrates against corrosion, as well as walls and monuments against graffiti. If they are applied onto the screens of hand-held electronic devices, these materials may even reduce fingerprint and smudge deposition.[9,10] Thus, superamphiphobic coatings are very useful.

Although superamphiphobic coatings are useful, they are difficult to achieve because many organic liquids such as cooking oils have low surface tensions of ∼30 mN/m and they spread readily on many solid substrates. For a coating to be superamphiphobic, it needs to possess a low surface tension, a high surface roughness, and re-entrant surface features.[6,7,11] While surface tensions as low as ∼6.7 mN/m can be provided by fluorinated organic compounds or polymers,[12] roughness can be achieved by decorating a surface with nanoparticles. However, re-entrant surfaces required for the effective vertical pinning of oil droplets to prevent them from sagging into cracks or air pockets of a rough coating are difficult to prepare using the bottom-up or self-assembly approaches. Thus, reports on these surfaces have been rare.[13,14]

Re-entrant surfaces are surfaces that are found hidden under overhangs. Well hidden surfaces that are effective for vertically pinning oil droplets include the gills of a standing mushroom or the inside surface of an umbrella. These structures have been created using top-down approaches such as lithography[1−3,15,16] and anisotropic plasma etching.[17,18] While these periodic structures bearing highly efficient re-entrant surfaces have been used to gain a fundamental understanding of factors governing superamphiphobicity, these top-down approaches are not readily scaled up. Bottom-up methods to create re-entrant features for superamphiphobicity have included growing nanofibers onto or from a substrate,[19] electro-spinning nanofibers onto a substrate,[1] etching slanted nanochannels into a substrate,[20] growing bumps onto a surface,[4,21] and casting particles with a binder.[22−29] Of these different methods, the particle-casting method is the most convenient and easiest to scale up. In a coating cast from spherical particles, the re-entrant features occur on the bottom half of each sphere. These re-entrant surfaces are not as effective in pinning liquids vertically as the gills of a mushroom, for example, because a spherical surface has no sharp turning or bending points.

Despite their aforementioned disadvantages, fluorinated spherical particles can be spread over inherently rough substrates such as textiles and render these textiles super-

Received: November 13, 2013
Accepted: February 6, 2014
Published: February 6, 2014

   dx.doi.org/10.1021/am4051074 | ACS Appl. Mater. Interfaces 2014, 6, 2629−2638

amphiphobic[28,30−33] because roughness and re-entrant surfaces occur at similar length scales as those of the particles, textile fiber diameter, and thread diameter. On intrinsically flat substrates such as glass plates, films of these particles do not fare as well and possess reduced repellency against hexadecane, for example, which has a low surface tension of 27.5 mN/m.[25,26,28,29] The repellency of the particulate coatings deteriorates further after the particles were modified into bifunctional particles that possessed not only fluorinated units but also functional groups such as carboxyl and amino groups that possessed high surface energies.[24,26,29] While the cocasting of these bifunctional particles with a polymer binder or glue helped improve adhesion between different particles and between the particles and a coating substrate, a further reduction in oil repellency was noticed.[24,26] This reduction could be due to the formation, at low binder loading, of a conformal coating by the binder on the particle surfaces or over a portion of their surfaces. When higher binder contents are employed, the particles could lose their re-entrant surfaces due to formation of an encapsulating binder bulk surrounding the bottom half of the spheres and turns a re-entrant concave site into a convex site, thus diminishing the self-cleaning properties even further.[23] To ensure superamphiphobicity on flat substrates and to counteract the adverse effects introduced by bifunctionalization of particles or by binders, particles possessing more complex architectures, and thus, better intrinsic oil repellency than that rendered by the simple fluorinated spheres are required.

A raspberry-like (RB) particle is a cluster composed of a larger spherical particle surrounded by many smaller spherical particles.[22−24] These particles should be intrinsically more effective than simple spherical particles in preparing superamphiphobic coatings for two reasons. First, these hierarchical dual-sized particles provide higher degrees of surface roughness. Second, each RB particle has many re-entrant surfaces associated with the bottom halves of the constituent particles rather than a single re-entrant surface provided by a simple spherical particle. While RB particles whose surfaces were functionalized with poly(dimethyl siloxane)[34] or with dodecyltrichlorosilane[35] have indeed exhibited better water repellency than simple spherical particles, their enhanced oil repellency has not been demonstrated. In this report, we present the preparation of a new type of RB particles and a new random copolymer for particle fluorination. After fluorination, these RB particles were cast as particulate films and the liquid repellency of these films was compared with that of films prepared from the simple fluorinated particles.

The smaller particles (*s*-GMA) that we used as precursors for the RB particles contained glycidyl methacrylate (GMA) units and were prepared from the surfactant-free emulsion copolymerization of styrene (S), GMA, and the cross-linker divinyl benzene (DVB). Meanwhile, the larger *l*-GMA particles were prepared via surfactant-free seeded emulsion polymerization. The cores of the larger particles were prepared through the copolymerization of S and DVB (A→B, Scheme 1). Polymerizing GMA, S, and DVB onto these core particles yielded a GMA-based shell (B→C). The glycidyl or epoxide groups present on the surface of these particles were then converted to amino groups by reacting the epoxide units with an excess of 2,2′-(ethylenedioxy)bis(ethylamine) or EDEA (C→D), thus yielding the larger amino-bearing particles (*l*-NH_2). We subsequently prepared the RB particles by reacting an excess of the *s*-GMA particles with the *l*-NH_2 particles (D→E). After purification, the residual epoxide groups on the surrounding small particles were further converted into amino groups via reaction with EDEA.

Scheme 1. Schematic Illustration of the Procedure Used to Prepare the RB Particles

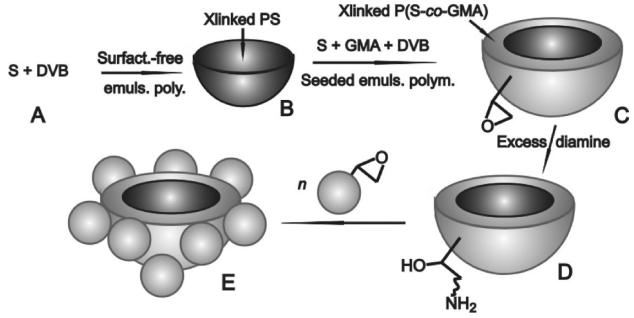

The fluorinating agent that we used was a statistical bifunctional copolymer of 2-(perfluorooctyl)ethyl methacrylate and glycidyl methacrylate or P(FOEMA-*co*-GMA) (Scheme 2), which was prepared via atom transfer radical polymerization (ATRP). While the FOEMA units provided the desired low-surface tension, particle fluorination was accomplished by reacting the GMA units with the amino groups on the surface of the RB particles. In addition, the unreacted residual GMA units of the copolymer should facilitate the covalent binding of these fluorinated particles to a glue if these particles are to be used in the future for fabricating mechanically robust coatings.[24,26,29]

Scheme 2. Chemical Structure of P(FOEMA-*co*-GMA)

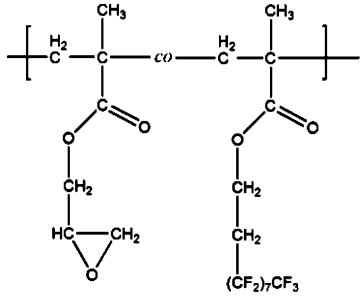

II. EXPERIMENTAL SECTION

Materials. All reagents used were purchased from Aldrich. Styrene (S, 99.9%), glycidyl methacrylate (GMA, 97%), and divinylbenzene (DVB, 80%) were purified by distillation under reduced pressure in a nitrogen atmosphere. The monomer 2-(perfluorooctyl)ethyl methacrylate (FOEMA, 97%, Aldrich) was purified via vacuum distillation over calcium hydride. 2,2′-Azobis(2-methylpropionamidine) dihydrochloride (V50, 97%), 2,2′-(ethylenedioxy)bis(ethylamine) (EDEA, 98%), ethyl α-bromoisobutyrate (98%), 2,2′-dipyridine (99%), cuprous bromide (CuBr, 98%), *N*,*N*-dimethylformamide (DMF, 99.8%), α,α,α-trifluorotoluene (TFT, 99%), tetrahydrofuran (THF, 99.9%), and methanol (99.8%) were used as received.

Epoxy-Functionalized Small (*s*-GMA) Particles. The small epoxy-bearing PS (*s*-GMA) particles were prepared from surfactant-free emulsion copolymerization of styrene (S), glycidyl methacrylate (GMA), and divinyl benzene (DVB). In a typical preparation, 0.30 g of GMA and 25.0 mL of deionized water were placed in a 125 mL two-neck round-bottom flask and deoxygenated under stirring by bubbling the solution with nitrogen gas for 10 min before 1.00 g of S and 50.3 mg of DVB were added into the flask. The mixture was then heated to 90 °C, and 40.1 mg of the initiator V50 (which had been predissolved

dx.doi.org/10.1021/am4051074 | ACS Appl. Mater. Interfaces 2014, 6, 2629−2638

in 5.0 mL of deionized water) was added to the reaction flask. The solution was left to react for 3 h under nitrogen protection before the emulsion was filtered through an absorbent cotton sheet (Premium Cotton Balls, Cotton) to remove aggregates. The filtrate was centrifuged at 17000 *g* for 10 min to settle the particles and the supernatant was decanted. The particles were redispersed into 1.5 mL of DMF and centrifuged to settle them again before the supernatant was discarded. The rinsing procedure was repeated once more. Subsequently, the precipitate was redispersed into 1.5 mL of THF and centrifuged again at 17 000*g* for 10 min to separate the supernatant. The settled particles were dried under vacuum to give 0.969 g of the product at a 74% yield.

Epoxy-Functionalized Large (*l*-GMA) Particles. Seeded emulsion polymerization was used to prepare the large epoxy-bearing (*l*-GMA) particles. To prepare the seed particles, 1.00 g of S, 50.2 g of DVB, and 25.0 mL of deionized water were added into a 125 mL two-neck round-bottom flask under nitrogen flow and heated to 75 °C. Subsequently, 30.2 mg of the initiator V50 (which had been predissolved in 5.0 mL of deionized water) was added. The solution was left to react for 4 h to yield the seed particles. Afterward, 1.00 g of S, 0.30 g of GMA, and 50.2 mg of DVB were added into the reaction flask and the solution was left to react for another 12 h. The *l*-GMA particles were purified using analogous procedures to those used to purify the *s*-GMA particles, except that the centrifugation force used was weaker at 9600*g*. Eventually, 1.452 g of the *l*-GMA particles were obtained in a 63% yield.

Amino-Functionalized Large (*l*-NH_2) Particles. To convert the epoxy-functionalized *l*-GMA particles to amino-functionalized *l*-NH_2 particles, 1.50 g of EDEA was dissolved in 10.0 mL of DMF and heated to 70 °C. Subsequently, 50 mg of the epoxy-functionalized *l*-GMA particles were added dropwise under vigorous stirring. The mixture was left to react overnight. The resultant particles were purified using a procedure similar to that described above for purifying the *l*-GMA particles except that the filtration step was skipped. This procedure provided 40.3 mg of the purified *l*-NH_2 particles.

Ninhydrin Test. A ninhydrin test was performed to confirm the presence of amino groups on the *l*-NH_2 particles. For this test, 50 mg of the *l*-NH_2 particles were initially redispersed into 0.2 mL of DMF. To this solution was then added 0.2 mL of an aqueous 2.2×10^{-3} M ninhydrin solution. The resultant mixture was heated at 70 °C for 2 min. A visual color change from clear to purple indicated the presence of amino groups.

Raspberry-like (RB) Particles. To prepare the RB particles, 25.0 mg of the *s*-GMA particles were dispersed into 4.0 mL of DMF and heated to 70 °C. To this solution was then added dropwise under vigorous stirring 5.0 mg of the *l*-NH_2 particles (which were predispersed into 1.0 mL of DMF). The mixture was stirred overnight. The resultant particles were then centrifuged at 600*g* for 10 min to settle the RB particles, and the excess *s*-GMA particles remaining in the supernatant were decanted. The RB particles were redispersed into 1.5 mL of DMF and centrifuged to remove the supernatant. This redispersion and centrifugation process was repeated another time. Lastly, the precipitate was redispersed into 1.5 mL of THF and centrifuged to settle the particles. These particles were subsequently dried under vacuum to yield 13.2 mg of target RB particles.

P(FOEMA-*co*-GMA). To prepare P(FOEMA-*co*-GMA), 26 mg (1.3×10^{-1} mmol) of ethyl α-bromoisobutyrate, 136 mg (0.96 mmol) GMA, 2.00 g (3.8 mmol) of FOEMA, 63 mg (0.40 mmol) of 2,2′-dipyridine, and 4.0 mL of trifluorotoluene were mixed in a two-neck round-bottom flask. The flask was degassed using nitrogen before 20 mg (0.14 mmol) of CuBr was added under a nitrogen flow. Subsequently, the flask was degassed via three freeze–pump–(nitrogen refill)–thaw cycles. The flask was then inserted into an oil bath that was preheated to 80 °C, and the polymerization was allowed to proceed for 2 h. The polymerization was quenched by immersing the flask into a liquid nitrogen bath and exposing its contents to air. The copper catalyst was removed by passing the solution through an alumina column using trifluorotoluene as the eluent. After the filtrate was concentrated to 3.0 mL via rotary evaporation, it was added into 20 mL of methanol in order to precipitate the copolymer. After the supernatant had been decanted, the copolymer was redissolved in 3.0 mL of trifluorotoluene and precipitated from 20 mL of methanol again. This procedure was repeated one more time before the solid was dried under vacuum for 24 h to provide 1.64 g of the copolymer at a 77% yield.

P(FOEMA-*co*-GMA) Characterization. A Waters 515 size exclusion chromatograph (SEC) equipped with a 2419 differential refractive index detector operating at 40 °C was used for P(FOEMA-*co*-GMA) molecular weight analysis. The column containing 5-μm 1000 Å AM gel from the American Polymer Standards Corporation was calibrated with monodisperse polystyrene standards. Trifluorotoluene was used as the mobile phase at a flow rate of 1.00 mL/min. ^{1}H NMR analysis was performed using a Bruker Advance 400 MHz spectrometer. The polymer was dissolved in a hexafluorobenzene/$CDCl_3$ mixture at v/v = 4/1.

Particle Fluorination. Initially, the residual epoxide groups of the *s*-GMA particles that had been grafted onto the *l*-NH_2 particles were reacted with EDEA to convert them into amino groups. To accomplish this, 1.50 g of EDEA was dissolved into 10 mL of DMF and the solution was heated to 70 °C. Under vigorous stirring, a 3.0 mL DMF solution containing 50 mg of the RB particles was added dropwise to the mixture. The resultant mixture was left to react overnight before the resultant particles were centrifuged at 600*g* for 10 min in order to settle the particles and to decant the supernatant. Subsequently, the particles were redispersed into 12 mL of DMF and centrifuged at 600*g* before the supernatant was discarded. This rinsing step was repeated once. The precipitate was then redispersed into 1.5 mL of THF and centrifuged for 10 min to settle the particles. The particles were dried under vacuum to give 43.3 mg of product.

The amino-functionalized RB particles (15.0 mg) were dispersed into 0.1 mL of DMF and diluted to 1.0 mL with TFT. The solution was then added dropwise into 2.0 mL of a vigorously stirred TFT solution containing 25 mg/mL of P(GMA-*co*-FOEMA) at 70 °C. The solution was left to react overnight before it was centrifuged at 17 000*g* for 10 min to settle the fluorinated particles and the supernatant was discarded. After redispersion into a 1.0 mL TFT/DMF mixture at v/v = 1/1, the particles were settled again and the rinsing solvent was discarded. Subsequently, the particles were redispersed into 0.6 mL of TFT and resettled via centrifugation. The precipitate was dried under vacuum to provide 25 mg of product.

Small *s*-GMA particles (50 mg) were converted to *s*-NH_2 particles by following a similar procedure as described above to give 42.2 mg of the particles. The *s*-NH_2 particles (15.0 mg) were then fluorinated with P(GMA-*co*-FOEMA) to provide 30 mg of the fluorinated particles.

Fluorinated Coatings. Glass plates were covered with fluorinated coatings consisting of P(FOEMA-*co*-GMA), the fluorinated *s*-NH_2 particles, and the fluorinated RB particles. In each case, 15 mg of the coating material was dispersed into 0.6 mL of TFT and then cast onto glass plate to cover an area of ~5.0 cm^2. The TFT was allowed to evaporate at room temperature from the cast solution to yield the final coatings.

Microscopic Analyses. In preparation for microscopic analyses, the *s*-GMA and *l*-GMA particles as well as the various RB particles were redispersed into THF at 1.0 mg/mL. They were then aero-sprayed onto carbon-coated TEM Cu grids or silicon wafers and dried under ambient conditions for 2 h prior to characterization via transmission electron microscopy (TEM) and atomic force microscopy (AFM). While TEM characterization was performed using a Hitachi H-7000 instrument operated at 75 kV, a Veeco Multimode instrument equipped with a Nanoscope IIIa controller operated in the tapping mode was used for AFM analysis. Rectangular-shaped silicon probes (AppNano, ACT) with a 300 kHz resonance frequency and a spring constant of 40 N/m were used for AFM characterization. Samples for scanning electron microscopy (SEM) were also aero-sprayed onto silicon wafers, coated with Au, and then analyzed using a Philips XL-30 ESEM FEG instrument that was operated at 2 kV.

Dynamic Light Scattering (DLS). The *s*-GMA and *l*-NH_2 particles as well as the RB particles were redispersed into DMF at 1.0 mg/mL in preparation for DLS characterization. Prior to analysis,

the *s*-GMA particles were filtered using a 0.45 μm filter, the *l*-NH_2 particles were filtered using a 1.2 μm filter, and the RB particles were centrifuged at 10*g* for 5 min. DLS analyses were performed at 21 °C at 90° using a Brookhaven BI-200 SM instrument equipped with a BI-9000AT digital correlator and a He−Ne laser. The data were analyzed using the Cumulant method to yield the hydrodynamic diameters (d_h) and the polydispersity indices (K_2/K_1^2) of the particles. The DMF refractive index and viscosity values used for these calculations were 1.4305 and 0.94 mPa·s, respectively.[36]

Contact Angle Measurements. Static contact angles were measured at room temperature using 5 μL of diiodomethane (>99%, Aldrich) or 10 μL of water, corn-based cooking oil (Mazola), or hexadecane (>99%, Aldrich) as the test liquids. Images of the liquid droplets were captured using a Canon PowerShot A700 camera and processed using the ImageJ software package.[37] Each reported contact angle represented the average of five measurements that were performed at different positions on the surface.

Sliding angles were measured using a home-built apparatus that is depicted in the Supporting Information (SI, Figure S1) using 10 μL droplets that were tested at five different positions on each sample. A coated glass plate was affixed to a ruler with double-sided adhesive tape. While one end of the ruler was placed against a horizontal metal block, the other end was placed on the top edge of a lab jack. After a liquid droplet was placed on the coated glass plate, the slope of the ruler was gradually increased by raising the lab jack, causing the ruler to tilt until the droplet began to roll. The sliding angle corresponded to the minimum angle of inclination required for a droplet placed on the substrate to roll off the surface.

Shedding angles on coated glass plates were also measured with the home-built apparatus mentioned above (SI, Figure S2) using 10 μL droplets. In this case, the droplets were dispensed from 1.0 cm above the substrate onto five different positions along the same horizontal line on each sample. The horizontal line was 2.0 cm above the bottom end of the glass plate. Measurements started at an initial inclination angle of 50 °, and this angle was gradually decreased. The shedding angle was recorded as the minimum angle of inclination below which one or more out of the five released droplets would no longer roll off the plate.

III. RESULTS AND DISCUSSION

s-GMA Particles. The *s*-GMA particles were prepared by the surfactant-free emulsion polymerization of S with GMA using V50 (Scheme 3) as the initiator and DVB as the cross-linker. Glycidyl methacrylate was used to introduce epoxide groups to the particles. Meanwhile, DVB served to ensure the stuctural integrity of the synthesized spheres in solvents such as DMF. V50 was chosen as the initiator because a V50 molecule decomposed into two radicals and the charged V50 fragments were mainly incorporated at the ends of linear segments of the polymer network. The charged end-groups provided electrostatic stabilization for the polymerized spheres and eliminated the need for additional surfactant. The elimination of surfactant from the reaction should have also facilitated the access of the epoxide units by amino groups during the intersphere coupling reaction to produce the targeted RB particles.

Scheme 3. Chemical Structures of V50 and GMA

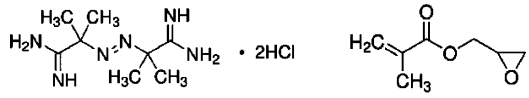

V50

GMA

Emulsion polymerization is a well-established technique and has been used industrially to prepare homopolymers or copolymers of methacrylates, acrylates, and styrenes.[38] The incorporation of DVB and GMA can be somewhat challenging. For example, we discovered that the DVB content could not exceed ~8 wt %. When the DVB content exceeded ~8 wt %, a precipitate was produced rather than well-dispersed spheres. Moreover, the epoxide groups of GMA might undergo ring-opening by water under basic or acidic conditions at high temperatures or by the amino groups present in the initiator. However, these side reactions should not be significant, since there have been literature reports on the emulsion polymerization of GMA with other monomers.[39−42] For example, Kling et al. synthesized polydisperse epoxy-functionalized PS particles from GMA and S using potassium persulfate (KPS) as the initiator.[39] The particle size distribution was improved by Lv et al., who used V50 as the initiator.[40] Furthermore, the use of V50 as the initiator yielded particles that retained more of their epoxy groups because the high-temperature decomposition of KPS produced protons as a side product and thus decreased the pH of the reaction medium. In the case of V50, the polymerization occurred under approximately neutral conditions. The amino groups of V50 could react with GMA. However, under the polymerization conditions most of the amino groups existed in the protonated or salt form. Thus, only a small amount of the epoxy rings would be opened during this polymerization.

The prepared particles were separated from the supernatant via centrifugation and rinsed twice with DMF and once with THF by dispersing the particles in the rinsing solvent and then separating them from the solvent by centrifugation and decantation. These particles were finally dispersed into THF, which was chosen as the solvent due to its lower boiling point and faster evaporation rate as compared to DMF. The solution was subsequently aero-sprayed using a home-built device[43] onto carbon-coated copper grids for TEM analysis and onto silicon wafers for AFM analysis. Figure 1a and b show the respective TEM and AFM images of these *s*-GMA particles.

The TEM and AFM images revealed that the particles were spherical, smooth, and narrow in size distribution (Table 1). Our statistical analysis of 50 *s*-GMA particles from different images yielded an average TEM diameter of 120 ± 4 nm, where 4 nm corresponded to the spread in the particle diameter instead of the typical standard deviation in the measurement. Previous researchers have concluded that S/GMA copolymer particles with a GMA content of 15−17 wt % possessed a spherical morphology and smooth surfaces. However, as the GMA content was increased to 40−43 wt %, particles became rough and irregular due to an increase in the polar content of the particles.[39−41] Our *s*-GMA particles were narrowly distributed because they had a relatively low GMA content of 23 wt %.

The narrow distribution of these particles was also confirmed by AFM. Our statistical analysis of ~50 particles from different images yielded an average AFM diameter of 180 ± 6 nm. The ~3% spread in the particle TEM and AFM diameters was typical for particles prepared via emulsion polymerization.[44] The AFM diameter was higher due to a contribution to the final value from the finite size of the AFM tip. We further obtained an average AFM height of 120 ± 5 nm for these particles. This value was consistent with the TEM diameter, suggesting that the particles were not significantly flattened during AFM specimen preparation.

The particles were also analyzed by DLS in DMF to yield a hydrodynamic diameter (d_h) of 212 ± 2 nm and a polydispersity of 0.053. While the low polydispersity value agreed with results obtained via TEM and AFM character-

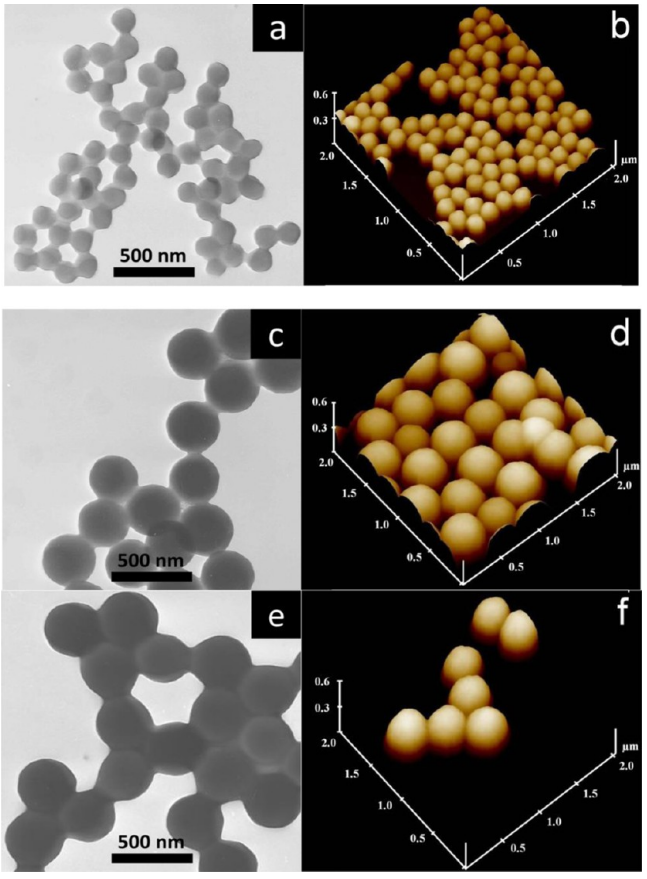

Figure 1. (a) TEM and (b) AFM topography images of *s*-GMA particles, (c) TEM and (d) AFM topography images of *l*-GMA particles, and (e) TEM and (f) AFM topography images of *l*-NH_2 particles.

Table 1. Size and Polydispersity of the Various Particles

particles	d_{TEM} (nm)[a]	d_{AFM} (nm)[a]	d_h (nm)[b]	K_2/K_1^2
s-GMA	120 ± 4	180 ± 6	212 ± 2	0.053
l-GMA	332 ± 10	390 ± 17		
l-NH_2	337 ± 10	420 ± 21	444 ± 5	0.050
RB	576 ± 24	780 ± 35	648 ± 9	0.183

[a]The numbers after "±" denote the spreads in the particle diameter. [b]The numbers after "±" denote the standard deviations.

ization, the diameter was substantially larger than those measured by TEM and AFM. The TEM and AFM diameters were smaller because they corresponded to the diameters of the dried particles. However, those determined by DLS represented the solvated particles. Additionally, the d_h value corresponded to the scattering-intensity-average diameter, also known as the *z*-average diameter, which should be higher than the number-average diameters determined via TEM and AFM.

***l*-GMA and *l*-NH_2 Particles.** The *l*-GMA particles were prepared in two steps. Initially, PS seed particles were prepared via soap-free emulsion polymerization of S using V50 as the initiator and DVB as the cross-linker. Next, more of the S monomer, DVB, and GMA were added to prepare a shell layer. Seeded polymerization was employed to produce larger particles as well as to ensure that the epoxy groups were located at or very near the surface of these large particles.

The dropwise addition of a DMF dispersion containing the *l*-GMA particles into an 2,2′-EDEA solution yielded amino-functionalized *l*-NH_2 particles. The principal reaction in this case should involve the opening of the epoxide rings by the amino groups (Scheme 4). The *l*-GMA particles were added slowly to ensure that EDEA always existed in a large excess and thus to minimize the chance for each EDEA molecule to react with two glycidyl groups. While the reaction of each EDEA molecule with two glycidyl groups within the same particle increased the degree of cross-linking of this particle, the reaction with two glycidyl groups from different particles should induce interparticle cross-linking. In both cases, no primary amino groups would be produced for further reaction and these processes should thus be avoided.

The techniques used to prepare the *s*-GMA specimens were also used to prepare the specimens of the *l*-GMA and *l*-NH_2 particles for TEM and AFM characterization. Figure 1c and d show the respective TEM and AFM images of the *l*-GMA particles, while Figure 1e and f show the respective TEM and AFM images of the *l*-NH_2 particles. The particles were predominantly spherical and smooth. While the average TEM and AFM diameters of the *l*-GMA particles were 332 ± 10 and 390 ± 17 nm, respectively, the correpoding values observed for the *l*-NH_2 particles were 337 ± 10 and 420 ± 21 nm. We further characterized the *l*-NH_2 particles in DMF via DLS and obtained a DLS diameter of 444 ± 5 nm and a polydispersity of 0.050, respectively. The polydispersity of these particles was low. Once again, the diameter obtained by DLS was larger than the microscopic diameters due to reasons explained in the previous subsection.

We also obtained diffuse reflectance infrared spectra of the *s*-GMA and *l*-GMA particles and these spectra are shown in Figure S3 in the SI. The spectra clearly confirmed that these particles bore epoxide rings. After these particles were reacted with EDEA, the presence of amino groups in the *l*-NH_2 particles was confirmed by a ninhydrin test (SI, Figure S4).

RB Particles. We prepared the RB particles by covalently linking together the *s*-GMA and *l*-NH_2 particles. This coupling reaction involved the opening of GMA epoxide rings by the amino groups. Since the amino-bearing *l*-NH_2 particles had many more amino groups per sphere than the two amino groups of EDEA, *l*-NH_2 should act as a cross-linker between different *s*-GMA particles. To minimize this particle network formation, we added a dispersion of the *l*-NH_2 particles dropwise into a vigorously stirred *s*-GMA dispersion at 70 °C. The high temperature was used to ensure that the ring-opening reaction occurred quickly, while *l*-NH_2 was added slowly to ensure that a large excess of the *s*-GMA particles existed during the majority of the coupling process and thus to facilitate the preparation of the targeted RB particles rather than a cross-linked network of particles.

In addition, an appropriate particle mixing molar ratio was important to maximize the RB particle yield and to minimize

Scheme 4. Reaction between *l*-GMA Particles and EDEA

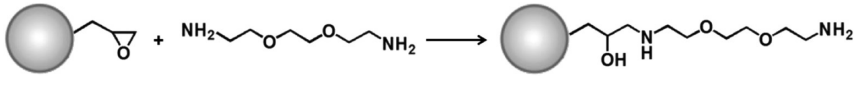

dx.doi.org/10.1021/am4051074 | ACS Appl. Mater. Interfaces 2014, 6, 2629−2638

particle cross-linking. Assuming a dense packing of the small particles with radius R_s on the surface of the large particles with radius R_l, Minami et al.[45] derived the relationship shown in eq 1 to calculating the maximum number of small particles, N_{max}, that could be accommodated on each large particle:

$$N_{max} = \frac{2\pi}{\sqrt{3}}\left(\frac{R_s + R_l}{R_s}\right)^2 \quad (1)$$

Inserting the TEM radii of 169 and 60 nm for the large and small particles, respectively, we calculated a N_{max} value of 53 for our system. In practice, we always used a feed mass ratio of 5:1 or a feed molar ratio of 100:1 for the *s*-GMA:*l*-NH_2 particle mixture unless otherwise mentioned. Therefore, an excess of the *s*-GMA particles were used to ensure successful RB particle preparation.

The need for a large excess of the *s*-GMA particles was confirmed by preparing particles using different *s*-GMA:*l*-NH_2 feed molar ratios that were increased from 2:1 to 20:1 and then to 40:1. At the first two feed molar ratios, a precipitate formed as the predominant product, thus suggesting that the RB particles were bridged by *s*-GMA particles. Meanwhile, the product consisted mainly of discrete RB particles when a feed molar ratio of 40:1 was employed, despite the fact that this ratio was still <53:1 (TEM image shown in SI, Figure S5). Our success in this case can be attributed to the slow addition of the *l*-NH_2 particles into the solution of the *s*-GMA particles. Furthermore, the complete coverage of the *l*-NH_2 particles by *s*-GMA particles was not necessary to prevent the RB particles from becoming cross-linked. The key was to ensure that the gaps in the encapsulating *s*-GMA layer of a RB particle were sufficiently small to prevent an *s*-GMA particle that was attached to another *l*-NH_2 particle from accessing the core *l*-NH_2 particle.

The prepared RB particles were purified and redispersed in THF. The particles were then aero-sprayed from THF for TEM and SEM analysis. To enhance contrast, the specimens used for SEM analysis were coated with a thin Au layer. The TEM and SEM images of these particles are shown in Figura 2a and b, respectively, while their AFM image is shown in Figure S6 in the SI.

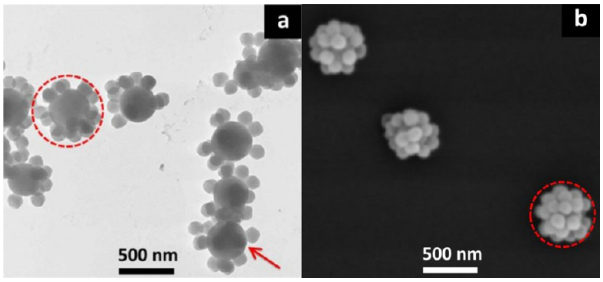

Figure 2. (a) TEM and (b) SEM images of the RB particles. The dotted circles were used to measure the RB particle diameters. The arrow shows a RB particle on which *s*-GMA particles can be seen as dark patches in the central *l*-NH_2 particle.

The raspberry-like shape of the particles was evident from the SEM images. On the other hand, the TEM image gave a "false" impression because only the *s*-GMA particles on the side of the central *l*-NH_2 particle were clearly visible and the *s*-GMA particles onto the front and back faces of each *l*-NH_2 particle were not clearly visible. This appearance was reasonable because the core *l*-NH_2 particle was significantly larger and scattered the electron beam much more effectively than the *s*-GMA particles. Consequently, the *s*-GMA particles that were grafted onto the front or back surfaces of an *l*-NH_2 particle should be either invisible or appear as dark patches, which were clearly visible on the face of the RB particle that is marked by an arrow in Figure 2a.

Our statistical analysis yielded respective TEM and SEM diameters of 565 ± 22 and 568 ± 25 nm for the RB particles. The TEM and SEM diameters were obtained by measuring and averaging the diameters of the smallest circles, such as the two dotted circles shown in Figure 2, that enclosed the RB particles. The RB particles dispersed in DMF were also analyzed by DLS to yield a d_h value of 648 ± 9 nm and a polydispersity index of 0.183. The DLS diameter was once again larger than the diameter measured by TEM and SEM for the reasons mentioned above for the precursory particles. In addition, the high polydispersity index may be due to the presence of some dimers or trimers of the RB particles as well as unreacted residual *s*-GMA particles.

Amino-Functionalized RB Particles. The RB particles bore residual glycidyl groups on the coronal *s*-GMA particles. We converted the residual glycidyl groups into amino groups by applying the same protocols that we had used to convert *l*-GMA to *l*-NH_2. This conversion was performed to facilitate the fluorination of the RB particles. Furthermore, we also prepared small amino-bearing *s*-NH_2 particles by reacting the *s*-GMA particles with EDEA.

P(FOEMA-*co*-GMA). A bifunctional random copolymer P(FOEMA-*co*-GMA) was used to fluorinate the RB particles.[28] We chose this polymer because its FOEMA units are highly water- and oil-repellent. In addition, the copolymer's GMA units would readily react with the amino groups that resided on the RB particle surfaces. We further suspected that some residual glycidyl groups would be present on the fluorinated particles to facilitate the binding of these bifunctional particles with a polymer binder. While classical free radical copolymerization could have been used to prepare this copolymer, we used atom transfer radical polymerization (ATRP) for this synthesis in order to yield a sample with a well-defined molecular weight and a low polydispersity.

The synthesized P(FOEMA-*co*-GMA) polymer was characterized via SEC using TFT as the eluent, and exhibited a single SEC peak at 6.2 min (SI, Figure S7). The polydispersity index (M_w/M_n) was 1.15 with respect to polystyrene standards. P(FOEMA-*co*-GMA) was also characterized via ^{1}H NMR spectroscopy, and its ^{1}H NMR spectrum as well as the corresponding signal assignments are shown in Figure 3. Signals *b* and *g* were taken as the representative peaks for the FOEMA and GMA units, respectively. Signal *b* corresponded to two protons, while peak *g* corresponded to one proton and the ratio between the integration of signals *b* and *g* is 8:1. Thus, the ratio between the number of FOEMA units and the GMA units was 4:1, indicating that the FOEMA units comprised 80 mol % of the copolymer's composition. In order to calculate the copolymer's number of repeat units, the integration of the H−C−Br signal corresponding to the initiator end group at 4.0 ppm in the ^{1}H NMR spectrum was compared to integration of signal *g* corresponding to the GMA unit. It was thus found that the copolymer incorporated 5 GMA units and 20 FOEMA units, resulting in a total number of 25 repeat units.

Particle Fluorination. We fluorinated the amino-bearing RB particles and some *s*-NH_2 particles by adding the particles

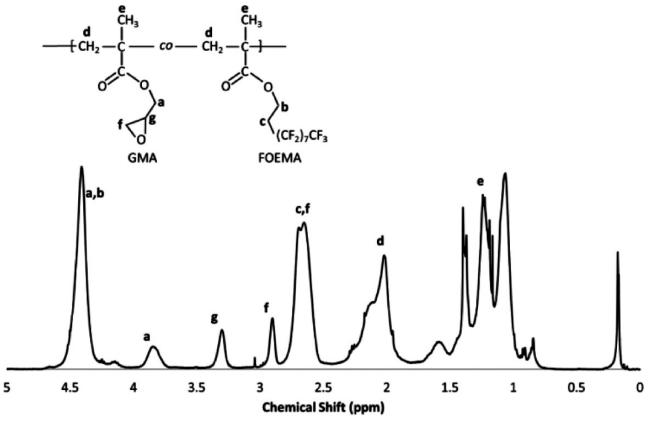

Figure 3. ^{1}H NMR spectrum and peak assignments for P(FOEMA-*co*-GMA) (400 MHz, 4:1 hexafluorobenzene/$CDCl_3$).

separately into solutions containing excess P(FOEMA-*co*-GMA). The fluorinated particles were then centrifuged to separate them from the unreacted P(FOEMA-*co*-GMA), which remained in the supernatant.

The amine-functionalized RB particles and *s*-NH particles were initially well-dispersed in DMF. After fluorination, however, the resultant particles became insoluble in this solvent. Instead, the resultant particles were readily dispersed into trifluorotoluene (TFT), a good solvent for P(FOEMA-*co*-GMA), suggesting successful fluorination of these particles.

Fluorinated Coatings. Coatings were prepared by casting TFT solutions of P(FOEMA-*co*-GMA), fluorinated *s*-NH_2 particles, and fluorinated RB particles onto glass plates and subsequently evaporating the solvent at room temperature. The resultant coatings were then observed directly by AFM or by SEM after Au plating. Figures 4 and 5 show the AFM and SEM images, respectively, of the resultant coatings.

A striking feature of the SEM and AFM images was that the fluorinated *s*-NH_2 particles were packed hexagonally locally. This symmetry, however, was missing from the RB coating. The uniformly sized fluorinated *s*-NH_2 particles crystallized into layered grains with defects at the grain boundaries. The RB-based coating did not exhibit a regular packing probably because of the fluctuation in the number of *s*-NH_2 particles per RB particle and thus the irregularity in the structure of the RB particles. This structural irregularity produced a rougher coating despite the use of the same particle casting protocol for the two types of particles.

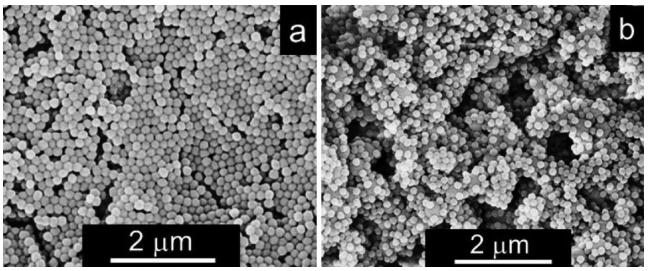

Figure 5. SEM images of coatings of (a) fluorinated *s*-NH_2 particles and (b) fluorinated RB particles that were cast onto glass plates.

The roughness of the coatings increased progressively from those of P(FOEMA-*co*-GMA), to those of the fluorinated *s*-NH_2 particles, and finally to those of the fluorinated RB particles. The root-mean-square roughness (R_{rms}) of these surfaces was measured with AFM imaging software over different areas of the samples using an image size of 2.0 × 2.0 μm^2. In the case of P(FOEMA-*co*-GMA) films, the R_{rms} value was 0.83 ± 0.7 nm, which was indicative of a flat surface. The R_{rms} value for the fluorinated *s*-NH_2 particle-based coatings was 51 ± 7 nm, as would be expected for a much rougher surface. Finally, the R_{rms} value for the fluorinated RB particle-based coatings was much higher than those exhibited by the other samples, at 102 ± 16 nm. This again would be anticipated due to the nature of the film, which consisted of particle clusters.

Liquid Repellency of the Fluorinated Coatings. Photographs of droplets of water, diiodomethane, corn-based cooking oil, and hexadecane sitting on glass plates coated with P(FOEMA-*co*-GMA), fluorinated *s*-NH_2 particles, and fluorinated RB particles are shown in Figure 6. Fitting the shapes of these droplets using the ImageJ software yielded the droplet contact angles, which are tabulated in Table 2. To better characterize the dynamic properties of these droplets, we also measured the sliding and shedding angles of these liquids on the different coatings and these results are also summarized in Table 2.

The data shown in Figure 6 and summarized in Table 2 suggest a number of expected trends: First, the liquid contact angle increased while the liquid rolling and shedding angles decreased progressively as the films were changed from those based on P(FOEMA-*co*-GMA) to those that were based on fluorinated *s*-NH_2 and then to films based on the fluorinated RB particles. Second, the droplet contact angle for a given coating decreased and the rolling or shedding angle increased as the surface tension decreased from 72.9 mN/m for water,[46] to 50.9 mN/m for diiodomethane,[47] to 33.8 mN/m for corn-

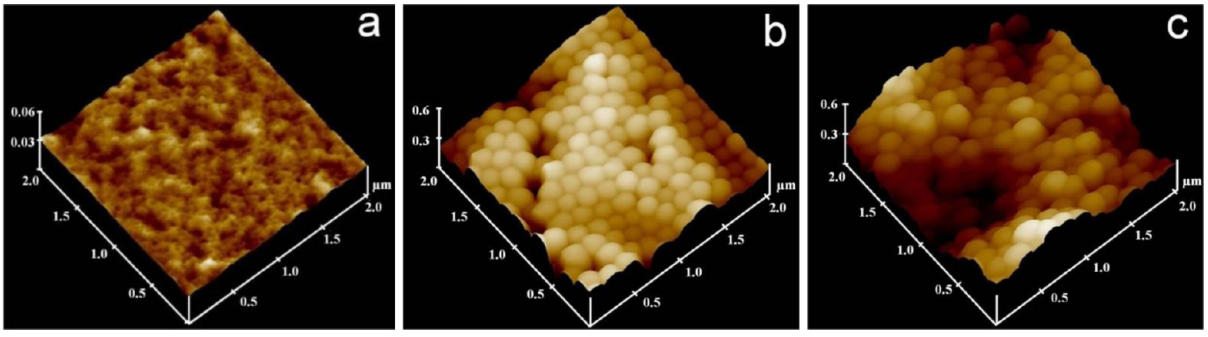

Figure 4. AFM topography images of coatings consisting of (a) P(FOEMA-*co*-GMA), (b) fluorinated *s*-NH_2 particles, and (c) fluorinated RB particles that were cast onto glass plates.

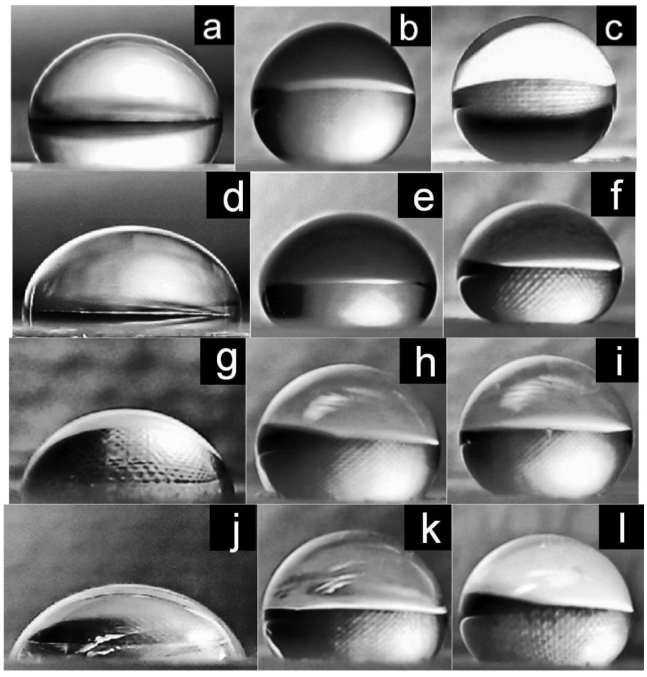

Figure 6. Photographs of droplets of (a–c) water, (d–f) diiodomethane, (g–i) corn-based cooking oil, and (j–l) hexadecane sitting on glass plates coated with (first column: a, d, g, j) P(FOEMA-*co*-GMA), (second column: b, e, h, k) fluorinated *s*-NH_2 particles, and (third column: c, f, i, l) fluorinated RB particles.

based cooking oil,[48] and to 27.5 mN/m for hexadecane.[46] The decrease in contact angles with decreasing liquid surface tension was readily understood. As the surface tension of a liquid decreased, the energy required to spread the liquid also decreased. Consequently, the contact angle of the liquid decreased.

The Wenzel and the Cassie theories can be used to explain why the contact angle of water or diiodomethane increased as the coating roughness increased. First, by assuming that the bottom of a liquid droplet was in full contact with the substrate, Wenzel related the observed liquid contact angle θ_b on a rough substrate with the intrinsic contact θ_0 of the liquid on a flat substrate of the same composition by eq 2:[49]

$$\cos\theta_b = R_f \cos\theta_0 \quad (2)$$

where the roughness R_f was originally defined by Wenzel as the ratio between the area of a rough surface with respect to that of its projected geometric surface area. More recent experiments have suggested that Rf should be more correctly[50] defined as the ratio between the length of the boundary line and the length of its projected curve. Since R_f is always larger than 1 and the water or diiodomethane droplets have intrinsic contact angles θ_0 larger than 90 ° on flat P(FOEMA-*co*-GMA) surfaces, an increase in R_f should cause θ_b to increase relative to θ_0 as observed experimentally.

The assumed Wenzel state involving the full contact between the bottom of a droplet and the substrate is not necessarily valid, particularly when $\theta_0 > 90$ ° or if the liquid has a low affinity for the substrate. In this case, the droplet may hang over protrusions and trap air pockets below the droplet to assume the so-called Cassie state. In the Cassie state, θ_b and θ_0 are related by eq 3:[51]

$$\cos\theta_b = R_f f_1 \cos\theta_0 - 1 + f_1 \quad (3)$$

where f_1 is the ratio of the projected length of the liquid/solid contact line segments at the droplet boundary to the total projected length of the droplet boundary line. Evidently, eq 3 reduces to eq 2 in the extreme case of $f_1 \rightarrow 1$. In the other extreme, when $f_1 \rightarrow 0$, eq 3 gives θ_b 180 °, which correctly gives the droplet/air contact angle for a spherical droplet. Since f_1 decreases as R_f increases, the Cassie theory also suggests that increasing R_f causes θ_b to increase.

Since cooking oil and hexadecane both exhibit $\theta_0 < 90$ °, eq 2 suggested that θ_b should be smaller than θ_0 in these cases. Furthermore, θ_b should decrease as R_f increases. Thus, the Wenzel theory could not explain the observed θ_b variation trend with R_f for these two liquids. On the other hand, the observed trend could still be explained by eq 3, suggesting that these droplets could still remain fully suspended over the protrusions (in the Cassie state) or only partially sagged into the protrusions of a rugged surface (in an intermediate state between the Cassie and Wenzel states). Liquids with such a high affinity for surfaces could still remain fully or partially suspended in the presence of re-entrant surfaces.[1−3] Scheme 5 shows the cross sections of trapezoids that lack re-entrant sites and inverted trapezoids that possess such sites. Since $\theta_0 < 90$°, the solid can be wetted by the liquid and thus the downward movement of the liquid/air/solid triphase contact line may occur in both cases a and b (represented by Scheme 5a and b,

Scheme 5. Cross-Sectional View of Liquid/Solid Contact on Two Rough Surfaces[a]

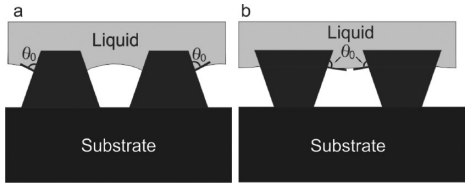

[a]The roughness is introduced by trapezoids that lack re-entrant surfaces in case (a) and by inverted trapezoids with re-entrant surfaces in case (b).

Table 2. Static Contact Angles (CA), Sliding Angles (A) and Shedding Angles Observed for Deionized Water, Diiodomethane, Corn-Based Cooking Oil, and Hexadecane on Coated Glass Plates[a]

	water			diiodomethane			corn cooking oil			hexadecane		
sample	static CA (deg)	sliding A (deg)	shedding A (deg)	static CA (deg)	sliding A (deg)	shedding A (deg)	static CA (deg)	sliding A (deg)	shedding A (deg)	static CA (deg)	sliding A (deg)	shedding A (deg)
P(FOEMA-*co*-GMA)	121 ± 2	N/A	45 ± 2	95 ± 1	15 ± 3	12 ± 1	90 ± 1	35 ± 1	35 ± 1	72 ± 3	17 ± 2	17 ± 2
s-NH_2	148 ± 5	<1	<1	138 ± 2	6 ± 1	4 ± 1	136 ± 3	N/A	N/A	132 ± 2	N/A	N/A
RB particles	165 ± 2	<1	<1	155 ± 3	<1	<1	152 ± 4	7 ± 2	7 ± 2	143 ± 1	13 ± 2	13 ± 2

[a]N/A: No angles were recorded. The droplet did not roll off the material even at a 90° tilting angle.

respectively). In case (a), the downward movement of the triphase contact line increases f_1 but decreases θ_b, leading to a spontaneous transition from the Cassie state to the Wenzel state, which normally has a smaller θ_b than that of the Cassie state. In case (b), on the other hand, the downward movement of the triphase contact line decreases f_1 but increases θ_b. Thus, the downward movement of the triphase contact line causes θ_b of the Cassie state to deviate further away from the θ_b value of the Wenzel state. Therefore, the Cassie-to-Wenzel state transition is not spontaneous. Rather, an activation energy is required for the transition and the re-entrant surface features keep the low surface-tension liquids in the Cassie state or in an intermediate state between the Cassie and Wenzel states. In these states, the contact angles increase as R_f increases in agreement with the results obtained for the cooking oil and hexadecane droplets.

Table 2 further demonstrates that water did not slide off the P(FOEMA-*co*-GMA) films even when the sample was tilted to 90°. However, the water droplets rolled off this film when it was placed at slanting angle of 45° or larger when they were dropped onto the surface from a height of 1.0 cm. The droplet could not readily slide or roll because of the lateral pinning of the droplets by the substrate. This pinning energy was evidently sufficiently small that it could be overcome by the initial kinetic energy provided to the falling droplet during the shedding angle measurement. This difference in the initial kinetic energy of a moving and a static droplet also explained why the rolling angles were higher than the shedding angles for diiodomethane in certain cases.

The lateral pinning of droplets is normally associated with the compositional and structural heterogeneity of a surface and a strong interaction between the droplet and the substrate.[15,16] Rough surfaces are structurally heterogeneous. Therefore, a droplet sitting on a rough surface in the Wenzel state or in a state involving extensive contact between the bottom of the droplet and the substrate would most likely be pinned and exhibit large sliding or shedding angles because of the surface structural heterogeneity and the large adhesion force between the droplet and the substrate. Being in such a state would explain why the cooking oil and hexadecane did not roll or slide off the fluorinated *s*-NH_2 coatings. Meanwhile, they did slide or exhibited lower rolling and shedding angles on the flat P(FOEMA-*co*-GMA) coatings because the latter surfaces had less structural heterogeneity. However, the shedding and rolling angles decreased sharply on the fluorinated RB particle surfaces. This decrease must have been caused by a reduction in the extent of contact with the substrate and thus a reduced adhesion force between the droplet bottom and the coating. Therefore, the droplets that sat on the RB coatings most likely existed in the Cassie state.

The most striking results of Table 2 were that the RB-based coatings applied onto a flat glass substrate were superoleophobic with regards to cooking oil. In addition, it was nearly so for hexadecane as well, despite this liquid's extremely low surface energy. While superoleophobicity has been achieved by creating overhanging structures using top-down approaches such as lithography on a flat substrate[1−3,15,16] or by casting fluorinated particles onto rough substrates such as textiles,[28,30−32] the results reported here represent the best superamphiphobicity achieved so far on flat substrates from the particle-casting approach.

IV. CONCLUSIONS

Surfactant-free emulsion polymerization and surfactant-free seeded emulsion polymerization techniques were used to prepare cross-linked *s*-GMA and *l*-GMA particles. Opening the epoxide rings of the GMA units of the *l*-GMA particles via reaction with the diamine EDEA converted the epoxide groups to amino groups. The slow addition of a dispersion of the resultant *l*-NH_2 particles into a dispersion of excess *s*-GMA particles yieled RB particles. The residual GMA units in the coronal *s*-GMA particles of the RB particles were also converted to amino groups via reaction with EDEA. Finally, fluorinated RB particles were prepared by grafting P(FOEMA-*co*-GMA) chains onto the amino-bearing RB particles. Since all of the preparations were performed under mild conditions, these procedures should be readily scalable. While only one type of RB particle has been prepared through the reported method, this method should be sufficiently general to accommodate the preparation of functional RB particles for other applications.

Casting dispersions of P(FOEMA-*co*-GMA), fluorinated *s*-NH_2 particles, and fluorinated RB particles onto glass plates and subsequently evaporating the solvent yielded fluorinated coatings. Under identical film formation conditions, the smoothest and roughest coatings were obtained from P(FOEMA-*co*-GMA) and fluorinated RB particles, respectively. The water and oil repellency of these films also improved in this order. On the fluorinated RB particle-based coatings, the static contact angle and rolling angle for water reached 165 ± 2° and <1°, respectively. Thus, the coating was superhydrophobic. Even low surface tension liquids such as cooking oil and hexadecane readily rolled off the RB-based coatings. Therefore, the RB coating was also strongly oleophobic. These results suggest that the RB particles are useful for preparing superamphiphobic self-cleaning surfaces on flat substrates through the bottom-up particle-casting approach.

■ ASSOCIATED CONTENT

Supporting Information

Videos showing cooking oil and diiodomethane droplets rolling off a glass plate coated with fluorinated raspberry-like particles. The droplets were dispensed from 1.0 cm above the substrate. Schematic diagrams of the home-built apparatus for measuring sliding and shedding angles. Diffuse reflectance infrared spectra of *s*-GMA and *l*-GMA particles. Photographs of vials containing *l*-NH_2 particles dispersed into deionized water before and after reaction with ninhydrin. TEM image of RB particles prepared at a number ratio of 40:1 for the *s*-GMA and *l*-NH_2 particles. AFM image of RB particles prepared at a number ratio of 100:1 for the *s*-GMA and *l*-NH_2 particles. SEC trace of P(FOEMA-*co*-GMA). This material is available free of charge via the Internet at http://pubs.acs.org.

■ AUTHOR INFORMATION

Corresponding Author

*E-mail: gliu@chem.queensu.ca.

Notes

The authors declare no competing financial interest.

■ ACKNOWLEDGMENTS

This work was funded by the Natural Sciences and Engineering Research Council of Canada (NSERC). G.L. wishes to thank the Canada Research Chair program for a Tier I Canada Research Chair Position in Materials Science.

REFERENCES

(1) Tuteja, A.; Choi, W.; Ma, M. L.; Mabry, J. M.; Mazzella, S. A.; Rutledge, G. C.; McKinley, G. H.; Cohen, R. E. *Science* **2007**, *318*, 1618−1622.
(2) Tuteja, A.; Choi, W. J.; McKinley, G. H.; Cohen, R. E.; Rubner, M. F. *MRS Bull.* **2008**, *33*, 752−758.
(3) Tuteja, A.; Choi, W.; Mabry, J. M.; McKinley, G. H.; Cohen, R. E. *Proc. Natl. Acad. Sci. U.S.A.* **2008**, *105*, 18200−18205.
(4) Deng, X.; Mammen, L.; Butt, H. J.; Vollmer, D. *Science* **2012**, *335*, 67−70.
(5) Liu, K.; Tian, Y.; Jiang, L. *Prog. Mater. Sci.* **2013**, *58*, 503−564.
(6) Xue, Z.; Liu, M.; Lei, J. *J. Polym. Sci., Part B: Polym. Phys.* **2012**, *50*, 1209−1224.
(7) Kota, A. K.; Choi, W.; Tuteja, A. *MRS Bull.* **2013**, *38*, 383−390.
(8) Wong, T. S.; Kang, S. H.; Tang, S. K. Y.; Smythe, E. J.; Hatton, B. D.; Grinthal, A.; Aizenberg, J. *Nature* **2011**, *477*, 443−447.
(9) Hikita, M.; Tanaka, K.; Nakamura, T.; Kajiyama, T.; Takahara, A. *Langmuir* **2005**, *21*, 7299−7302.
(10) Kondo, H.; Sungkil, L.; Hanaoka, H. *Tribol. Lubr. Technol.* **2009**, *65*, 54−61.
(11) Butt, H. J.; Semprebon, C.; Papadopoulos, P.; Vollmer, D.; Brinkmann, M.; Ciccotti, M. *Soft Matter* **2013**, *9*, 418−428.
(12) Nishino, T.; Meguro, M.; Nakamae, K.; Matsushita, M.; Ueda, Y. *Langmuir* **1999**, *15*, 4321−4323.
(13) Grigoryev, A.; Tokarey, T.; Kornev, K. G.; Luzinov, I.; Minko, S. *J. Am. Chem. Soc.* **2012**, *134*, 12916−12919.
(14) Grigoryev, A.; Roiter, Y.; Tokarev, I.; Luzinov, I.; Minko, S. *Adv. Funct. Mater.* **2013**, *23*, 870−877.
(15) Zhao, H.; Park, K. C.; Law, K. Y. *Langmuir* **2011**, *28*, 14925−14934.
(16) Zhao, H.; Law, K. Y. *ACS Appl. Mater. Interfaces* **2012**, *4*, 4288−4295.
(17) Ellinas, K.; Tserepi, A.; Gogolides, E. *Langmuir* **2011**, *27*, 3960−3969.
(18) Fujii, T.; Aoki, Y.; Habazaki, H. *Langmuir* **2011**, *27*, 11752−11756.
(19) Zhang, J. P.; Seeger, S. *Angew. Chem., Int. Ed.* **2011**, *50*, 6652−6656.
(20) Cao, L. L.; Price, T. P.; Weiss, M.; Gao, D. *Langmuir* **2008**, *24*, 1640−1643.
(21) Xie, Q. D.; Xu, J.; Feng, L.; Jiang, L.; Tang, W. H.; Luo, X. D.; Han, C. C. *Adv. Mater.* **2004**, *16*, 302−305.
(22) Muthiah, P.; Bhushan, B.; Yun, K.; Kondo, H. *J. Colloid Interface Sci.* **2013**, *409*, 227−236.
(23) Campos, R.; Guenthner, A. J.; Meuler, A. J.; Tuteja, A.; Cohen, R. E.; McKinley, G. H.; Haddad, T. S.; Mabry, J. M. *Langmuir* **2012**, *28*, 9834−9841.
(24) Xiong, D. A.; Liu, G. J.; Zhang, J. G.; Duncan, E. J. S. *Chem. Mater.* **2011**, *23*, 2810−2820.
(25) Xiong, D. A.; Liu, G. J.; Hong, L. Z.; Duncan, E. J. S. *Chem. Mater.* **2011**, *23*, 4357−4366.
(26) Xiong, D. A.; Liu, G. J.; Duncan, E. J. S. *Polymer* **2013**, *54*, 3008−3016.
(27) Hsieh, C. T.; Wu, F. L.; Chen, W. Y. *J. Phys. Chem. C* **2009**, *113*, 13683−13688.
(28) Zhang, G. W.; Hu, J. W.; Liu, G. J.; Zou, H. L.; Tu, Y. Y.; Li, F.; Hu, S. Y.; Luo, H. S. *J. Mater. Chem. A* **2013**, *1*, 6226−6237.
(29) Xiong, D. A.; Liu, G. J.; Duncan, E. J. S. *ACS Appl. Mater. Interfaces* **2012**, *4*, 2445−2454.
(30) Zhou, H.; Wang, H. X.; Niu, H. T.; Gestos, A.; Lin, T. *Adv. Funct. Mater.* **2013**, *23*, 1664−1670.
(31) Wang, H. X.; Xue, Y. H.; Ding, J.; Feng, L. F.; Wang, X. G.; Lin, T. *Angew. Chem., Int. Ed.* **2011**, *50*, 11433−11436.
(32) Pan, S. J.; Kota, A. K.; Mabry, J. M.; Tuteja, A. *J. Am. Chem. Soc.* **2013**, *135*, 578−581.
(33) Leng, B. X.; Shao, Z. Z.; de With, G.; Ming, W. H. *Langmuir* **2009**, *25*, 2456−2460.
(34) Ming, W.; Wu, D.; van Benthem, R.; de With, G. *Nano Lett.* **2005**, *5*, 2298−2301.
(35) Qian, Z.; Zhang, Z.; Song, L.; Liu, H. *J. Mater. Chem.* **2009**, *19*, 1297−1304.
(36) Haynes, W. M. *CRC Handbook of chemistry and physics*, 94th ed.; CRC Press Taylor and Francis Group: Boca Raton, FL, 2013.
(37) Rasband, W. S. *ImageJ*; U.S. National Institutes of Health: Bethesda, MD, 1997−2012; http://imagej.nih.gov/ij/.
(38) Eliseeva, V. I.; Ivanchev, S. S.; Kuchanov, S. I.; Lebedev, A. V. *Emulsion polymerization and its applications in industry*; Consultants Bureau: New York, 1981.
(39) Kling, J. A.; Ploehn, H. J. *J. Polym. Sci., Part A: Polym. Chem.* **1995**, *33*, 1107−1118.
(40) Lv, J.-N.; Fang, S.-J.; Chen, L. *Chin. J. Polym. Sci.* **2009**, *27*, 101−108.
(41) Mouaziz, H.; Larsson, A.; Sherrington, D. C. *Macromolecules* **2004**, *37*, 1319−1323.
(42) Zurkova, E.; Bouchal, K.; Zdenkova, D.; Pebzbauer, Z.; Svec, F.; Kalal, J. *J. Polym. Sci., Polym. Chem. Ed.* **1983**, *21*, 2949−2960.
(43) Ding, J. F.; Liu, G. J. *Macromolecules* **1999**, *32*, 8413−8420.
(44) Gilbert, R. G. *Emulsion Polymerization: A Mechanistic Approach*; Academic Press: London, 1995.
(45) Minami, H.; Mizuta, Y.; Suzuki, T. *Langmuir* **2013**, *29*, 554−560.
(46) Jasper, J. J. *J. Phys. Chem. Ref. Data* **1972**, *1*, 841−1009.
(47) Korosi, G.; Kovats, E. S. Density and Surface Tension of 83 Organic Liquids. *J. Phys. Chem. Ref. Data* **1981**, *26*, 323−332.
(48) Esteban, B.; Riba, J.-R.; Baquero, B.; Puig, R.; Rius, A. *Fuel* **2012**, *102*, 231−238.
(49) Wenzel, R. N. *Ind. Eng. Chem.* **1936**, *28*, 988−994.
(50) Gao, L. C.; McCarthy, T. J. *Langmuir* **2007**, *23*, 3762−3765.
(51) Cassie, A. B. D.; Baxter, S. *Trans. Faraday Soc.* **1944**, *40*, 546−550.